Magnetization switching through giant spin–orbit torque in a magnetically doped topological insulator heterostructure

Yabin Fan[1]*[†], Pramey Upadhyaya[1][†], Xufeng Kou[1][†], Murong Lang[1], So Takei[2], Zhenxing Wang[1], Jianshi Tang[1], Liang He[1]*, Li-Te Chang[1], Mohammad Montazeri[1], Guoqiang Yu[1], Wanjun Jiang[1], Tianxiao Nie[1], Robert N. Schwartz[1], Yaroslav Tserkovnyak[2] and Kang L. Wang[1]*

Recent demonstrations of magnetization switching induced by in-plane current in heavy metal/ferromagnetic heterostructures (HMFHs) have drawn great attention to spin torques arising from large spin–orbit coupling (SOC). Given the intrinsic strong SOC, topological insulators (TIs) are expected to be promising candidates for exploring spin–orbit torque (SOT)-related physics. Here we demonstrate experimentally the magnetization switching through giant SOT induced by an in-plane current in a chromium-doped TI bilayer heterostructure. The critical current density required for switching is below 8.9×10^4 A cm^{-2} at 1.9 K. Moreover, the SOT is calibrated by measuring the effective spin–orbit field using second-harmonic methods. The effective field to current ratio and the spin-Hall angle tangent are almost three orders of magnitude larger than those reported for HMFHs. The giant SOT and efficient current-induced magnetization switching exhibited by the bilayer heterostructure may lead to innovative spintronics applications such as ultralow power dissipation memory and logic devices.

Recently, heavy metals (for example, Pt, Ta) with strong SOC have been used to generate spin currents by passing an in-plane charge current to control the magnetization dynamics in an adjacent ferromagnet layer (for example, Co, CoFeB; refs 1–12). Such spin currents, arising from either the spin-Hall effect[1–3,13,14] within the heavy metals or the Rashba effect at the interfaces[7–10,14–20], can apply efficient spin torques to the ferromagnet, and result in current-induced magnetization manipulation[2,6,7,9–12] and even switching[1,3,8]. Although the underlying mechanisms of the SOTs are still debated[1,4,14], the ability to manipulate magnetic moments with lateral current has shown promising applications in miniaturized magnetic memory and logic devices, and more appropriate material/structure to generate these SOTs still deserves further investigation. Besides heavy metals, TIs (refs 21–23), in which the SOC is large enough to invert the band structure[24], are expected to be the most promising candidates to exploit the SOTs when coupled to magnetic moments[25–27]. In addition, the recently demonstrated magnetism in magnetically doped TIs (for example, Cr-doped TIs; refs 28–34) makes it accessible to study the SOTs in the TI/magnetic-TI bilayer heterostructures[28,35]. Here, we demonstrate the magnetization switching by in-plane current injection into epitaxial TI/Cr-doped TI bilayer films. Using the second-harmonic analysis[4,5] of the anomalous Hall effect (AHE) resistance, we calibrate the effective spin–orbit field arising from the SOT. Most importantly, we find that the effective field to current ratio, as well as the spin-Hall angle tangent, is nearly three orders of magnitude larger than those reported in HMFHs so far. This giant SOT, together with the current-induced switching behaviour, suggests

that magnetically doped TI heterostructures could potentially be the materials/structures to generate SOTs with efficiency beyond today's HMFHs.

Results

Device structure and magnetic properties. Epitaxial $(Bi_{0.5}Sb_{0.5})_2Te_3/(Cr_{0.08}Bi_{0.54}Sb_{0.38})_2Te_3$ bilayer films are first grown on an insulating GaAs(111) substrate using the modulation-doped molecular beam epitaxy (MBE) growth method[28], as illustrated in Fig. 1a. The top $(Bi_{0.5}Sb_{0.5})_2Te_3$ layer thickness is chosen to be 3 quintuple layers and the bottom $(Cr_{0.08}Bi_{0.54}Sb_{0.38})_2Te_3$ layer is 6 quintuple layers, with atomically sharp hetero-interfaces in between as indicated by high-resolution scanning transmission electron microscopy (STEM; Supplementary Section 1). In this structure, the Bi/Sb ratio is adjusted to 0.5/0.5 in the top $(Bi_{0.5}Sb_{0.5})_2Te_3$ layer and 0.59/0.41 in the bottom $(Cr_{0.08}Bi_{0.54}Sb_{0.38})_2Te_3$ layer so that both layers exhibit similar conductivities (222.7 S cm^{-1} and 219.5 S cm^{-1}, respectively), which guarantees a uniform current distribution inside the entire structure (see Supplementary Section 1 for detailed electric properties)[28].

Pronounced ferromagnetism has recently been reported in $(Cr_xBi_ySb_{1-x-y})_2Te_3$ films[28,36], and with an appropriate doping concentration, the quantum anomalous Hall phase[33] is also obtained. To investigate the SOTs in our TI/Cr-doped TI heterostructure, micrometre-size Hall bar devices[37] were prepared, as shown in Fig. 1b. When applying a large enough external magnetic field B_{ext} in the yz plane, the magnetization M becomes polarized, and the relative positions between B_{ext} and M are illustrated in Fig. 1a, where θ_B and θ_M are the polar angles of

[1]Department of Electrical Engineering, University of California, Los Angeles, California 90095, USA, [2]Department of Physics and Astronomy, University of California, Los Angeles, California 90095, USA. [†]These authors contributed equally to this work. *e-mail: yabin@seas.ucla.edu; liang.heliang@gmail.com; wang@seas.ucla.edu
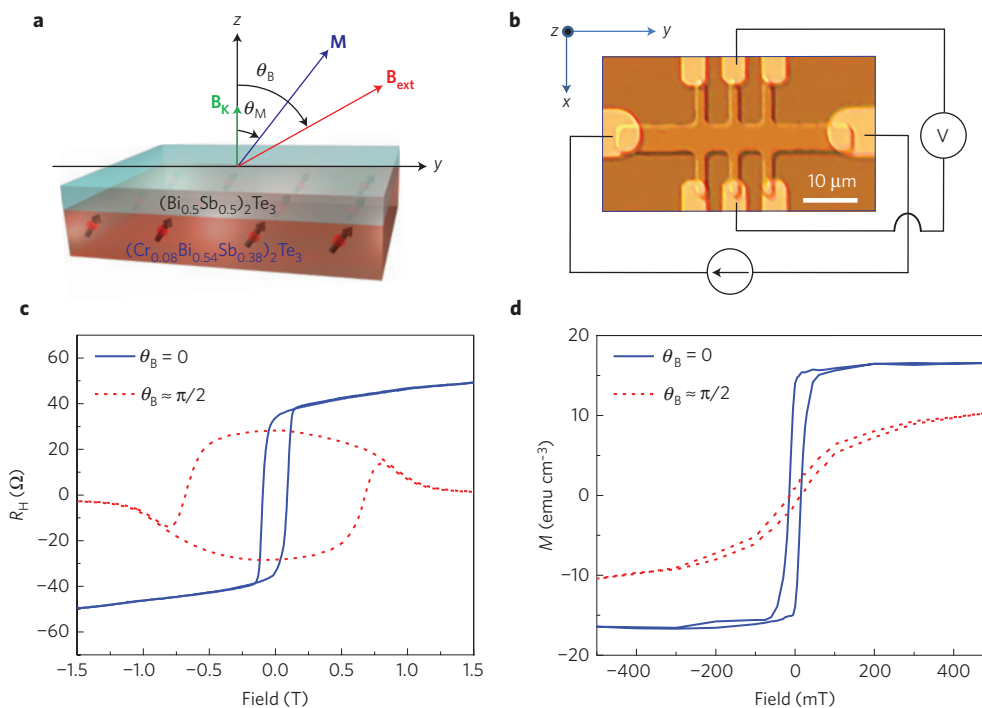
Figure 1 | Experimental set-up and magnetic properties of the $(Bi_{0.5}Sb_{0.5})_2Te_3/(Cr_{0.08}Bi_{0.54}Sb_{0.38})_2Te_3$ bilayer heterostructure. a, Three-dimensional schematic of the bilayer heterostructure. The top layer (light blue) shows the 3 quintuple layers $(Bi_{0.5}Sb_{0.5})_2Te_3$ and the bottom layer (light red) presents the 6 quintuple layers $(Cr_{0.08}Bi_{0.54}Sb_{0.38})_2Te_3$. **$B_{ext}$** (red arrow) represents the external magnetic field and **M** (blue arrow) denotes the magnetization of the bottom $(Cr_{0.08}Bi_{0.54}Sb_{0.38})_2Te_3$ layer. **B_K** (green arrow) is the out-of-plane anisotropy field. **b**, Micrograph of the Hall bar device with schematic illustrations of the Hall measurement set-up. The width of the Hall bar and the length between two neighbouring Hall contacts are both 5 μm. **c**, The Hall resistance as a function of the applied external magnetic field for both the out-of-plane ($\theta_B = 0$) and nearly in-plane ($\theta_B \approx \pi/2$) directions, respectively, at 1.9 K. **d**, Superconducting quantum interference device measurement of the magnetization for both the out-of-plane ($\theta_B = 0$) and in-plane ($\theta_B \approx \pi/2$) directions, respectively, at 5 K for external magnetic fields up to ±500 mT.

B_{ext} and **M** from the z axis, respectively. Here, $B_K = K\cos\theta_M\hat{z}$ is the out-of-plane anisotropy field with K being the anisotropy coefficient estimated to be around 0.9 T (Supplementary Section 2).

Field-dependent Hall resistance measurements of the TI/Cr-doped TI bilayer heterostructure for both the out-of-plane ($\theta_B = 0$) and nearly in-plane ($\theta_B \approx \pi/2$) directions were carried out at 1.9 K, and the results are shown in Fig. 1c. The nearly square-shape magnetic hysteresis loop of R_H at $\theta_B = 0$ clearly suggests that the magnetization easy axis is out-of-plane (that is, along the z direction). In addition, superconducting quantum interference device measurements were carried out to directly probe the magnetization **M** for both the out-of-plane ($\theta_B = 0$) and in-plane ($\theta_B \approx \pi/2$) directions, and the results are shown in Fig. 1d. The saturation magnetization M_S is measured to be around 16 emu cm^{-3} along the out-of-plane ($\theta_B = 0$) direction for applied magnetic fields greater than 100 mT. In contrast, **M** does not show any saturation behaviour even when $|B_{ext}| > 500$ mT for fields along the in-plane ($\theta_B \approx \pi/2$) direction, again indicating the robust out-of-plane magnetic anisotropy of our TI/Cr-doped TI heterostructure sample.

Magnetization switching induced by an in-plane current. In our conductive TI/Cr-doped TI bilayer heterostructure, a dominant spin accumulation in the Cr-doped TI layer with spin polarized in the transverse direction is expected when passing a charge current in the y direction due to the spin-Hall effect in the bulk and the spin polarization arising from the Rashba-type interactions at the interfaces. A strong enhancement of the interfacial spin accumulation can be expected due to the spin-momentum locking of the topological surface states[21,22,25,38,39]. The accumulated spins' angular momentum can be directly transferred to the magnetization

M and therefore affect its dynamics. In particular, such a SOT can be described as $\tau_{SO} = -\gamma M \times B_{SO}$, where the effective spin–orbit field is $B_{SO} = I\lambda_{SO}\hat{x} \times m$. Here γ is the gyromagnetic ratio, λ_{SO} is the coefficient characterizing the SOC strength in the system, I is the charge current conducting along the longitudinal direction and **m** is the unit vector that denotes the magnetization direction. This SOT is normally referred to as the spin transfer-like SOT (ref. 4), and the equally important field-like SOT term is found to be an order of magnitude smaller in our structure (Supplementary Sections 4 and 5). As a result, we focus mainly on the spin transfer-like SOT in the following. Accordingly, we illustrate the four stable states in Fig. 2a where the applied d.c. current, $I_{d.c.}$, conducts along the longitudinal direction (that is, $\pm y$ axis), and the external magnetic field is also applied along the $\pm y$ axis. In panel 1 of Fig. 2a, for example, we show the case where the d.c. current, $I_{d.c.}$, and the in-plane external magnetic field, B_y, are both applied along the $+y$ axis. The effective spin–orbit field, B_{SO}, induced by $I_{d.c.}$ is pointing along the tangential $-\hat{\theta}$ direction of **M**, which tilts **M** up to obtain a positive z component, M_z, when in equilibrium. The other three cases for different configurations of the applied $I_{d.c.}$ and B_y are illustrated in panels 2–4 of Fig. 2a, correspondingly. To summarize, in the presence of a constant external magnetic field in the y direction, the z-component magnetization M_z can be switched, depending on the d.c. current conduction direction[1,3,8]; likewise, when the applied d.c. current is fixed, M_z can also be switched by changing the in-plane external magnetic field.

On the basis of such a scenario, we carried out the ($I_{d.c.}$-fixed, B_y-dependent) and the (B_y-fixed, $I_{d.c.}$-dependent) experiments at 1.9 K; the results are shown in Fig. 2b,c, respectively. Specifically, when $I_{d.c.} = +10$ μA (blue squares in Fig. 2b), the AHE resistance R_{AHE} goes from negative to positive as the applied in-plane magnetic
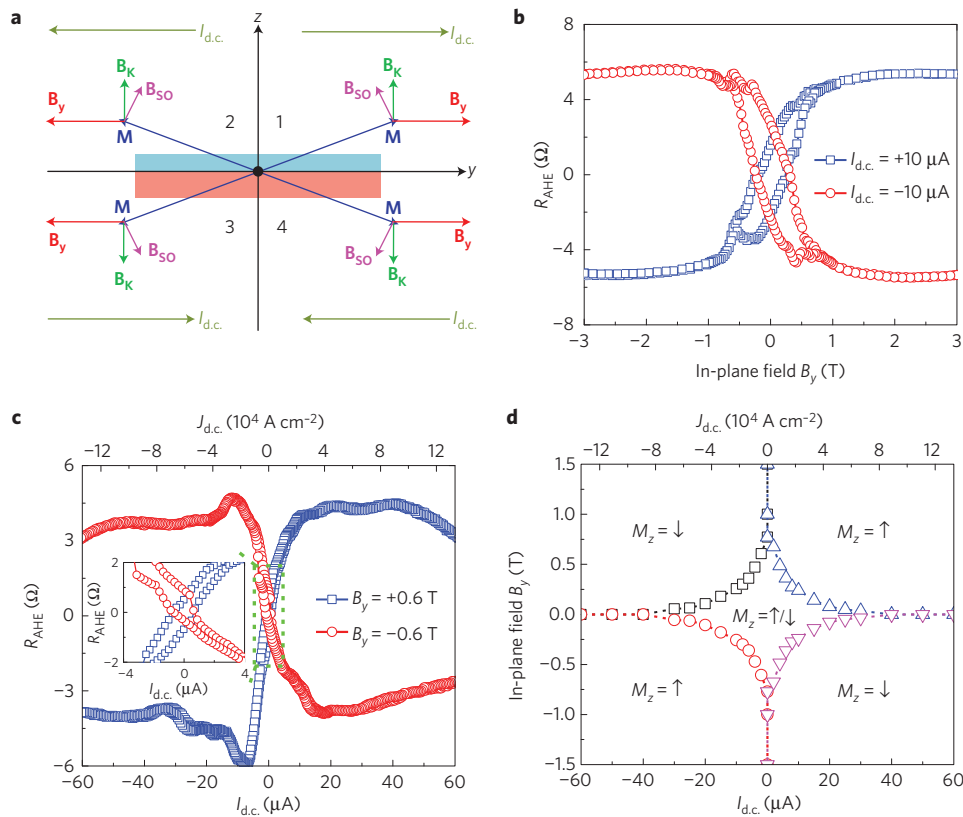
Figure 2 | Magnetization switching due to the SOT induced by an in-plane d.c. current. a, Schematic of the four stable magnetization states (panels 1–4) when passing a large d.c. current, $I_{d.c.}$, and applying an in-plane external magnetic field, $\mathbf{B_y}$, in the $\pm y$ directions. The effective spin–orbit field $\mathbf{B_{SO}}$ induced by the d.c. current and the anisotropy field $\mathbf{B_K}$ are both considered. **b**, The AHE resistance R_{AHE} as a function of the in-plane external magnetic field when passing a constant d.c. current with $I_{d.c.} = +10\,\mu A$ and $I_{d.c.} = -10\,\mu A$ along the Hall bar, respectively, at 1.9 K. **c**, Current-induced magnetization switching in the Hall bar device at 1.9 K in the presence of a constant in-plane external magnetic field with $B_y = +0.6\,T$ and $B_y = -0.6\,T$, respectively. Inset: Expanded scale to show the hysteresis windows. **d**, Phase diagram of the magnetization state in the presence of an in-plane external magnetic field $\mathbf{B_y}$ and a d.c. current $I_{d.c.}$. The dashed lines and symbols (obtained from experiments) represent switching boundaries between the different states. In all panels, the symbol $\uparrow$ means $M_z > 0$ and $\downarrow$ means $M_z < 0$, not $M_z = \pm M_S$.

field $\mathbf{B_y}$ gradually changes from $-3\,T$ to $3\,T$, indicating that the z-component magnetization M_z switches from $-z$ to $+z$. In contrast, when $I_{d.c.} = -10\,\mu A$, the AHE resistance reverses sign (red circles in Fig. 2b) and M_z varies from $+z$ to $-z$ as $\mathbf{B_y}$ is swept from $-3\,T$ to $3\,T$. It should be noted that in both cases the AHE resistance hysteresis loops agree well with our proposed scenario. At the same time, when we scan the d.c. current $I_{d.c.}$ at a given fixed magnetic field, we also observe similar magnetization switching behaviour: the AHE resistance R_{AHE} changes from negative to positive for $B_y = +0.6\,T$ (blue squares in Fig. 2c), but reverses its evolution trend, that is, changes from positive to negative, for $B_y = -0.6\,T$ (red circles in Fig. 2c). For this case, the small hysteresis window in R_{AHE} is clearly visible on an expanded scale as shown in the inset of Fig. 2c. Consequently, both the ($I_{d.c.}$-fixed, $\mathbf{B_y}$-driven) and the ($\mathbf{B_y}$-fixed, $I_{d.c.}$-driven) magnetization switching behaviours clearly demonstrate that the magnetization can be effectively manipulated by the current-induced SOT in our TI/Cr-doped TI bilayer heterostructure. We summarize these switching behaviours in the phase diagram in Fig. 2d. For the four corner panels in Fig. 2d where the field value B_y and $I_{d.c.}$ are large, the magnetization state is deterministic; however, in the central panel where B_y and $I_{d.c.}$ are small, both magnetization states, up and down, are possible; this behaviour agrees with the hysteresis windows, as shown in Fig. 2b,c, where in the low-B_y and small-$I_{d.c.}$ region the two magnetization states are both allowed. On the basis of this phase diagram, it can be clearly seen that the magnetization can be easily switched with only tens of micro-amperes of d.c. current

(that is, below $8.9 \times 10^4\,A\,cm^{-2}$ in current density $J_{d.c.}$), suggesting that the current-induced SOT in our TI/Cr-doped TI bilayer heterostructure is quite efficient. The temperature dependence of the critical switching current density and the anisotropy field can be found in Supplementary Section 7.

Second-harmonic analysis of the AHE resistance. To quantitatively analyse the current-induced SOT in the TI/Cr-doped TI bilayer system, we carried out harmonic measurements of the AHE resistance to calibrate the effective spin–orbit field $\mathbf{B_{SO}}$ arising from the SOT. By sending an a.c. current, $I_{a.c.}(t) = I_0 \sin(\omega t)$, into the Hall bar device, the alternating effective field, $\mathbf{B_{eff}}(t) = \mathbf{B_{SO}}\sin(\omega t)$, causes the magnetization $\mathbf{M}$ to oscillate around its equilibrium position, which gives rise to a second-harmonic AHE resistance (Supplementary Section 2): $R_{AHE}^{2\omega} = -\frac{1}{2}I_0 dR_{AHE}/dI$. The second-harmonic AHE resistance $R_{AHE}^{2\omega}$ contains information of the effective field $\mathbf{B_{SO}}$ and has been used as an effective method to quantify it[4,5]. Here we introduce two different ways to measure this effective field by the second-harmonic method[4], namely, one is to sweep the external magnetic field to large values, and the other one is to rotate the external magnetic field direction while keeping its magnitude fixed. Both ways give quantitatively the same effective field $\mathbf{B_{SO}}$ for a given a.c. current as discussed in detail below.

In Fig. 3 we show the second-harmonic AHE resistance $R_{AHE}^{2\omega}$ as a function of the in-plane external magnetic field when the input a.c. current is given as $I_{a.c.}(t) = I_0 \sin(\omega t)$, where $I_0 = 2\,\mu A$ and $\omega = 15.8\,Hz$ are used. When the in-plane external magnetic field is

larger than the saturation field (that is, $|B_y| > K$), the Cr-doped TI layer will be in a single-domain state and polarized in the same direction as $\mathbf{B_y}$, as illustrated in regions I and III in Fig. 3. In this state, the second-harmonic AHE resistance is given by the simple formula (Supplementary Section 3)

$$R_{AHE}^{2\omega} = -\frac{1}{2}\frac{R_A B_{SO}}{(|B_y| - K)} \qquad (1)$$

where $R_A = 36\,\Omega$ is the out-of-plane saturation AHE resistance. Under such circumstance, the magnetization $\mathbf{M}$ will be polarized and the oscillation magnitude induced by the a.c. current will decrease if we further increase B_y, thus causing $R_{AHE}^{2\omega}$ to scale as $1/(|B_y| - K)$. By fitting the $R_{AHE}^{2\omega}$ versus B_y curve in the large field region with the above formula, we find the effective field value, $B_{SO} \approx \pm 26.2\,\text{mT}$, pointing along $+z$ or $-z$ depending on the direction of $\mathbf{B_y}$, which is consistent with the definition of $\mathbf{B_{SO}}$. Consequently, the scaling relation of $R_{AHE}^{2\omega}$ confirms that the measured $R_{AHE}^{2\omega}$ signal indeed comes from the SOT-induced magnetization oscillation around its equilibrium position.

In addition to sweeping the external magnetic field, we also performed the field rotation experiments to find the angle dependence of the effective spin–orbit field. By continuously rotating the external magnetic field orientation in the yz plane while keeping its magnitude fixed at 2 T, we managed to effectively rotate the magnetization of the Cr-doped TI layer in the yz plane, while maintaining it in a single-domain state. Defining the clockwise direction as the positive rotation direction, as shown in the insets of Fig. 4a–c, the first- and second-harmonic AHE resistances, $R_{AHE}^{1\omega}$ and $R_{AHE}^{2\omega}$, were measured simultaneously[4,5], as a function of the field angle θ_B from $-\pi$ to π in the yz plane. The results are shown in Fig. 4a,b, respectively (to get the correct $R_{AHE}^{1\omega}$, the ordinary Hall resistance component has been subtracted from the total first-harmonic Hall resistance). In this case, the effective spin–orbit field, $\mathbf{B_\theta} = \mathbf{B_{SO}}$, induced by the a.c. current is pointing along the tangential direction of the magnetization $\mathbf{M}$. This field $\mathbf{B_\theta}$ is the origin of $R_{AHE}^{2\omega}$, according to (Supplementary Section 2):

$$R_{AHE}^{2\omega} = -\frac{R_A}{2B_{ext}\cos(\theta_B - \theta_M)}\frac{d(\cos\theta_M)}{d\theta_B}B_\theta \qquad (2)$$

At non-zero θ_B, the first-harmonic AHE resistance is given by $R_{AHE}^{1\omega} = R_A\cos\theta_M$. θ_M is a function of θ_B, and their relationship can be established by solving the equilibrium condition of the magnetization when applying an external magnetic field. For details, see Supplementary Section 2 (Supplementary equation (2.6)). Combining $R_{AHE}^{1\omega}$ and $R_{AHE}^{2\omega}$, we get $B_\theta = -2B_{ext}\cos(\theta_B - \theta_M)R_{AHE}^{2\omega}/(dR_{AHE}^{1\omega}/d\theta_B)$. Shown in Fig. 4c is the obtained effective spin–orbit field value B_θ as a function of the rotation angle θ_B for different amplitudes of the a.c. current, $I_{a.c.}$, ranging from 1 μA to 5 μA, respectively. Note that we get strictly negative values for B_θ, which means the effective field $\mathbf{B_\theta}$ is pointing towards the $-\hat{\theta}$ tangential direction (that is, anticlockwise). This is consistent with the magnetic field sweeping experiments shown in Fig. 3 and the current-induced switching data in Fig. 2c. Equally important, we observe that the effective field $\mathbf{B_\theta}$ is highly anisotropic, reaching the highest value at $\theta_B = 0, \pm\pi$ (out-of-plane) and lowest at $\theta_B = \pm\pi/2$ (in-plane). The θ_B dependence of the effective spin–orbit field reveals that the SOT anisotropy is stronger than those reported for the AlO$_x$/Co/Pt and MgO/CoFeB/Ta systems[4], possibly owing to the emergence of higher-order terms in the SOT expression[4] when considering the strong SOC in TIs.

In addition, we also plot the effective field value B_θ as a function of the a.c. current amplitude for three different θ_B angles, $\theta_B = 0, \pi/4$ and $\pi/2$, in Fig. 4d, respectively. The effective field
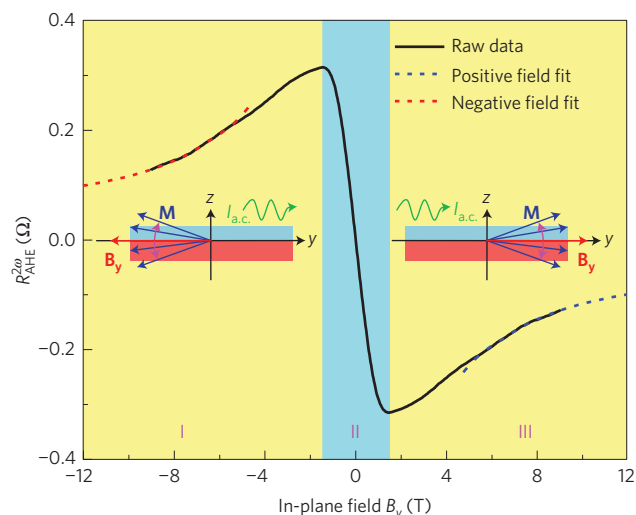

Figure 3 | Second-harmonic AHE resistance as a function of the in-plane external magnetic field. The shaded regions I, II and III represent a single-domain state pointing in the $-y$ direction, magnetization reversal, and a single-domain state pointing in the y direction, respectively. The solid black line is the experimental raw data. The dashed lines denote the fitting proportional to $1/(|B_y| - K)$ in the negative field region (red line) and in the positive field region (blue line), respectively. Insets in regions I and III show the magnetization oscillation around its equilibrium position when passing an a.c. current. The a.c. current amplitude is 2 μA and the frequency is 15.8 Hz.

$\mathbf{B_\theta}$ has a linear dependence on the a.c. current amplitude (or a.c. current density amplitude $J_{a.c.}$), and the $|B_\theta|/J_{a.c.}$ ratio ranges from $0.0048\,\text{mT}\,(\text{A cm}^{-2})^{-1}$ to $0.0146\,\text{mT}\,(\text{A cm}^{-2})^{-1}$, which is nearly three orders of magnitude larger than those reported in HMFHs (refs 4,5). Using the spin-Hall angle tangent[3,4], defined as $\vartheta_{SH} = 2eM_S B_\theta t_{Cr-TI}/\hbar J_{a.c.}$, where e is the electron charge, $\hbar$ is Planck's constant divided by 2π and t_{Cr-TI} is the Cr-doped TI layer thickness, to quantify the SOT, we find that the ϑ_{SH} value ranges from 140 to 425, depending on θ_B, which is almost three orders of magnitude larger than those reported in HMFHs. Here, ϑ_{SH} has the same sign as the one revealed in Pt (ref. 1). Again, this giant SOT observed in our TI/Cr-doped TI bilayer heterostructure is attributed to the strong SOC interaction in the whole structure and the coexisting magnetism, in conjunction with the breaking of the reflection symmetry in the growth direction by Cr doping. The topological surface states may play an important role in the current-induced SOT because of the spin-momentum locking mechanism, which is expected to be a much more efficient way to generate SOT compared with heavy metals[25]. The role of the topological surface states and the various associated spin-galvanic/magneto-electric phenomena discussed in refs 25,27,40,41 warrant additional and more elaborate experiments. For example, the harmonic measurements of the heterostructures with various top TI layer and bottom Cr-doped TI layer thicknesses should be carried out; however, that is beyond the scope of this paper.

We have demonstrated the magnetization switching by the ($I_{d.c.}$-fixed, $\mathbf{B_y}$-driven) and the ($\mathbf{B_y}$-fixed, $I_{d.c.}$-driven) experiments that reveal the giant SOT induced by the in-plane current in the TI/Cr-doped TI bilayer heterostructure. The switching is efficient, requiring a critical current density below $8.9 \times 10^4\,\text{A cm}^{-2}$ at 1.9 K. We further analysed the current-induced SOT by extracting the effective spin–orbit field using second-harmonic measurement of the AHE resistance. We found that the $|B_{SO}|/J_{a.c.}$ ratio, as well as the spin-Hall angle tangent ϑ_{SH}, is nearly three orders of magnitude larger than the ones reported so far in HMFHs. In addition, we showed that the SOT exhibits a strong angular anisotropy. Very
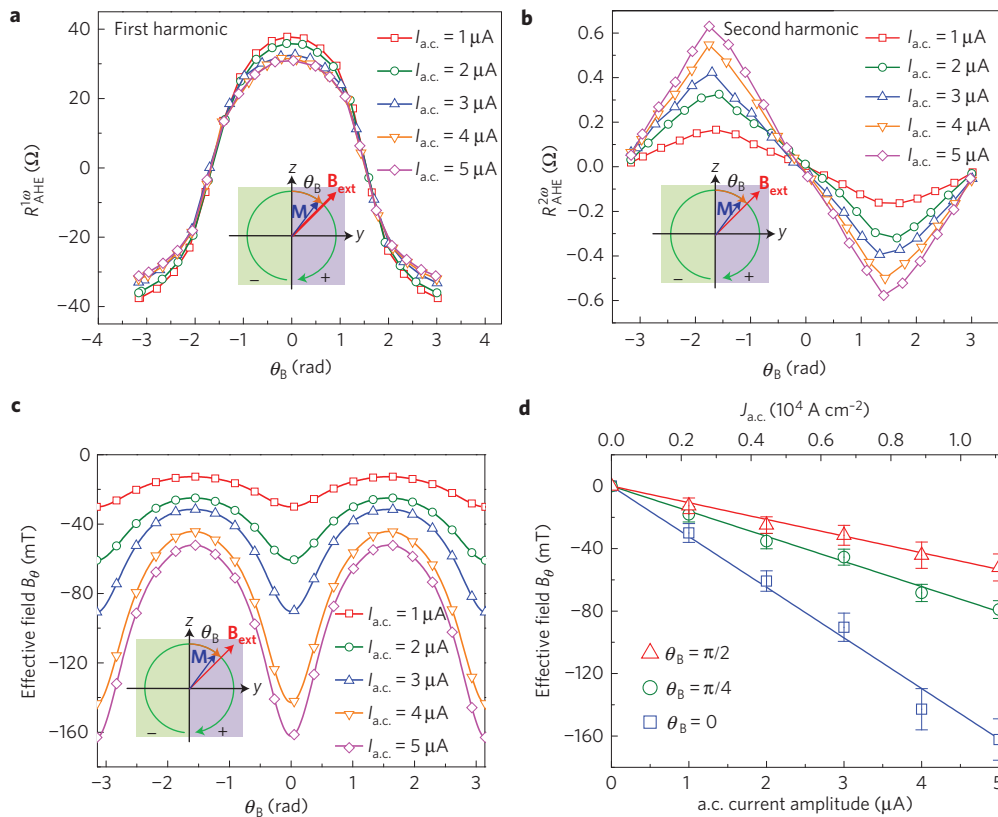
Figure 4 | Harmonic signals and effective spin–orbit fields obtained from the rotation experiments. **a,b**, First- and second-harmonic AHE resistances, $R_{AHE}^{1\omega}$ and $R_{AHE}^{2\omega}$, as a function of the field angle θ_B for the applied a.c. current $I_{a.c.}$ with different amplitudes ranging from $1\,\mu A$ to $5\,\mu A$, respectively, when θ_B varies from $-\pi$ to π in the yz plane as shown in the inset figures. **c**, The effective spin–orbit field as a function of θ_B for the applied a.c. current $I_{a.c.}$ with different amplitudes ranging from $1\,\mu A$ to $5\,\mu A$. **d**, The effective spin–orbit field as a function of the a.c. current amplitude $I_{a.c.}$ for three different θ_B angles, $\theta_B = 0, \pi/4$ and $\pi/2$. Straight lines are the linear fittings. Error bars show standard errors. In all the rotation experiments, the $\mathbf{B_{ext}}$ field magnitude is fixed at 2 T and the temperature is kept at 1.9 K.

recent work[42] reporting a spin torque ratio of up to 3.5 in the Bi_2Se_3/permalloy heterostructure at room temperature also suggests that TIs are good SOT source materials. The use of the giant SOT revealed in our TI/Cr-doped TI bilayer heterostructure for room-temperature applications will probably require a search for high-Curie-temperature magnetic TIs or other alternative room-temperature insulating (or high resistivity) magnetic materials that can couple efficiently with TIs. Therefore, our findings in the TI/Cr-doped TI bilayer heterostructure may spur further work on heterostructures that integrate TIs and magnetic materials, and may potentially lead to the innovation of novel SOT devices.

Methods

MBE growth. Thin-film growth was performed using an ultrahigh vacuum Perkin Elmer MBE system. Semi-insulating ($\rho > 10^6\,\Omega\,cm$) GaAs (111) substrates were pre-annealed in the growth chamber at up to $580\,°C$ to remove the native oxide. High-purity Bi (99.9999%), Te (99.9999%), Cr (99.99%) and Sb (99.999%) were evaporated by conventional effusion cells and cracker cells. During the modulation-doped growth, the GaAs (111) substrate was maintained at $200\,°C$ (growth temperature). Bi and Te cells were kept at $470\,°C$ and $320\,°C$, respectively, whereas the Sb and Cr temperatures were varied to adjust the carrier densities and the magnetic impurity doping profiles in different layers. Epitaxial growth was monitored by an *in situ* reflection high-energy electron diffraction (RHEED) technique, and the surface was found to be atomically flat as evidenced by streaky RHEED patterns. Digital images of the RHEED were captured using a KSA400 system built by K-space Associates.

Characterizations. High-resolution STEM experiments were performed on a FEI TITAN Cs-corrected STEM operating at $200\,kV$ and the high-angle annular dark field (HAADF) images were acquired using a Fischione HAADF detector. Four-point Hall measurements were conducted using the quantum design

physical property measurement system. We were able to systematically alter several experimental variables such as temperature, magnetic field, measurement frequency and external gate bias. Multiple lock-in-amplifiers and Keithley source meters were also connected with the physical property measurement system, enabling comprehensive and high-sensitivity transport measurements for the Hall bar devices.

Device fabrication. The modulation-doped $(Bi_{0.5}Sb_{0.5})_2Te_3/(Cr_{0.08}Bi_{0.54}Sb_{0.38})_2Te_3$ bilayer thin films were patterned into micrometre-scale Hall bar geometries using conventional optical photolithography with subsequent CHF_3 dry etching for 18 s. A 20-nm-thick high-k Al_2O_3 dielectric layer was deposited by atomic layer deposition at $250\,°C$. The Hall channel contacts were defined by electron-beam evaporation after the Al_2O_3 was etched away in the contact areas. A metal stack of Ti/Al (20 nm/100 nm) was directly deposited onto the exposed TI top surface to form the contacts.

References

1. Liu, L., Lee, O. J., Gudmundsen, T. J., Ralph, D. C. & Buhrman, R. A. Current-induced switching of perpendicularly magnetized magnetic layers using spin torque from the spin Hall effect. *Phys. Rev. Lett.* **109**, 096602 (2012).
2. Liu, L., Moriyama, T., Ralph, D. C. & Buhrman, R. A. Spin-torque ferromagnetic resonance induced by the spin Hall effect. *Phys. Rev. Lett.* **106**, 036601 (2011).
3. Liu, L. *et al.* Spin-torque switching with the giant spin Hall effect of tantalum. *Science* **336**, 555–558 (2012).
4. Garello, K. *et al.* Symmetry and magnitude of spin–orbit torques in ferromagnetic heterostructures. *Nature Nanotech.* **8**, 587–593 (2013).
5. Kim, J. *et al.* Layer thickness dependence of the current-induced effective field vector in Ta|CoFeB|MgO. *Nature Mater.* **12**, 240–245 (2013).

6. Suzuki, T. *et al.* Current-induced effective field in perpendicularly magnetized Ta/CoFeB/MgO wire. *Appl. Phys. Lett.* **98,** 142505 (2011).
7. Miron, I. M. *et al.* Current-driven spin torque induced by the Rashba effect in a ferromagnetic metal layer. *Nature Mater.* **9,** 230–234 (2010).
8. Miron, I. M. *et al.* Perpendicular switching of a single ferromagnetic layer induced by in-plane current injection. *Nature* **476,** 189–193 (2011).
9. Pi, U. H. *et al.* Tilting of the spin orientation induced by Rashba effect in ferromagnetic metal layer. *Appl. Phys. Lett.* **97,** 162507 (2010).
10. Miron, I. M. *et al.* Fast current-induced domain-wall motion controlled by the Rashba effect. *Nature Mater.* **10,** 419–423 (2011).
11. Ando, K. *et al.* Electric manipulation of spin relaxation using the spin Hall effect. *Phys. Rev. Lett.* **101,** 036601 (2008).
12. Haazen, P. P. J. *et al.* Domain wall depinning governed by the spin Hall effect. *Nature Mater.* **12,** 299–303 (2013).
13. Vedyayev, A., Strelkov, N., Chshiev, M., Ryzhanova, N. & Dieny, B. Spin transfer torques induced by spin Hall effect. Preprint at http://arxiv.org/abs/1108.2589v1 (2011).
14. Manchon, A. Spin Hall effect versus Rashba torque: A diffusive approach. Preprint at http://arxiv.org/abs/1204.4869 (2012).
15. Wang, X. & Manchon, A. Diffusive spin dynamics in ferromagnetic thin films with a Rashba interaction. *Phys. Rev. Lett.* **108,** 117201 (2012).
16. Pesin, D. A. & MacDonald, A. H. Quantum kinetic theory of current-induced torques in Rashba ferromagnets. *Phys. Rev. B* **86,** 014416 (2012).
17. Haney, P. M., Lee, H-W., Lee, K-J., Manchon, A. & Stiles, M. D. Current induced torques and interfacial spin–orbit coupling: Semiclassical modeling. *Phys. Rev. B* **87,** 174411 (2013).
18. Kim, K-W., Seo, S-M., Ryu, J., Lee, K-J. & Lee, H-W. Magnetization dynamics induced by in-plane currents in ultrathin magnetic nanostructures with Rashba spin–orbit coupling. *Phys. Rev. B* **85,** 180404 (2012).
19. Chernyshov, A. *et al.* Evidence for reversible control of magnetization in a ferromagnetic material by means of spin–orbit magnetic field. *Nature Phys.* **5,** 656–659 (2009).
20. Wang, X. & Manchon, A. Rashba spin torque in an ultrathin ferromagnetic metal layer. Preprint at http://arxiv.org/abs/1111.5466 (2011).
21. Qi, X-L. & Zhang, S-C. Topological insulators and superconductors. *Rev. Mod. Phys.* **83,** 1057–1110 (2011).
22. Hasan, M. Z. & Kane, C. L. Colloquium: Topological insulators. *Rev. Mod. Phys.* **82,** 3045–3067 (2010).
23. Moore, J. E. The birth of topological insulators. *Nature* **464,** 194–198 (2010).
24. Zhang, H. *et al.* Topological insulators in Bi_2Se_3, Bi_2Te_3 and Sb_2Te_3 with a single Dirac cone on the surface. *Nature Phys.* **5,** 438–442 (2009).
25. Fischer, M. H., Vaezi, A., Manchon, A. & Kim, E-A. Large spin torque in topological insulator/ferromagnetic metal bilayers. Preprint at http://arxiv.org/abs/1305.1328 (2013).
26. Mahfouzi, F., Nagaosa, N. & Nikolic, B. K. Spin-orbit coupling induced spin-transfer torque and current polarization in topological-insulator/ferromagnet vertical heterostructures. *Phys. Rev. Lett.* **109,** 166602 (2012).
27. Tserkovnyak, Y. & Loss, D. Thin-film magnetization dynamics on the surface of a topological insulator. *Phys. Rev. Lett.* **108,** 187201 (2012).
28. Kou, X. *et al.* Manipulating surface-related ferromagnetism in modulation-doped topological insulators. *Nano Lett.* **13,** 4587–4593 (2013).
29. Checkelsky, J. G., Ye, J., Onose, Y., Iwasa, Y. & Tokura, Y. Dirac-fermion-mediated ferromagnetism in a topological insulator. *Nature Phys.* **8,** 729–733 (2012).
30. Chen, Y. L. *et al.* Massive Dirac Fermion on the surface of a magnetically doped topological insulator. *Science* **329,** 659–662 (2010).
31. Wray, L. A. *et al.* A topological insulator surface under strong Coulomb, magnetic and disorder perturbations. *Nature Phys.* **7,** 32–37 (2011).
32. Chang, C-Z. *et al.* Thin films of magnetically doped topological insulator with carrier-independent long-range ferromagnetic order. *Adv. Mater.* **25,** 1065–1070 (2013).
33. Chang, C-Z. *et al.* Experimental observation of the quantum anomalous Hall effect in a magnetic topological insulator. *Science* **340,** 167–170 (2013).
34. Kou, X. F. *et al.* Magnetically doped semiconducting topological insulators. *J. Appl. Phys.* **112,** 063912 (2012).
35. He, L. *et al.* Surface-dominated conduction in a 6 nm thick Bi_2Se_3 thin film. *Nano Lett.* **12,** 1486–1490 (2012).
36. Kou, X. *et al.* Interplay between different magnetisms in Cr-doped topological insulators. *ACS Nano* **7,** 9205–9212 (2013).
37. Lang, M. *et al.* Revelation of topological surface states in Bi_2Se_3 thin films by *in situ* Al passivation. *ACS Nano* **6,** 295–302 (2012).
38. Yazyev, O. V., Moore, J. E. & Louie, S. G. Spin polarization and transport of surface states in the topological insulators Bi_2Se_3 and Bi_2Te_3 from first principles. *Phys. Rev. Lett.* **105,** 266806 (2010).
39. Hsieh, D. *et al.* A tunable topological insulator in the spin helical Dirac transport regime. *Nature* **460,** 1101–1105 (2009).
40. Garate, I. & Franz, M. Inverse spin-galvanic effect in the interface between a topological insulator and a ferromagnet. *Phys. Rev. Lett.* **104,** 146802 (2010).
41. Nomura, K. & Nagaosa, N. Electric charging of magnetic textures on the surface of a topological insulator. *Phys. Rev. B* **82,** 161401 (2010).
42. Mellnik, A. R. *et al.* Spin transfer torque generated by the topological insulator Bi_2Se_3. Preprint at http://arxiv.org/abs/1402.1124 (2014).

Acknowledgements

Author contributions

Y.F., P.U., X.K. and K.L.W. conceived and designed the research. X.K. and L.H. grew the material. M.L. fabricated the Hall bar devices. Y.F., P.U. and X.K. performed the measurements. M.L., Z.W., J.T., L.H., L-T.C., M.M., G.Y., W.J., T.N. and R.N.S. contributed to the measurements and analysis. X.K. and T.N. performed structural analysis. Y.F., P.U., S.T. and Y.T. designed the theoretical model. Y.F., P.U., X.K. and K.L.W. wrote the paper with help from all of the other co-authors.

Additional information

Supplementary information is available in the online version of the paper. Reprints and permissions information is available online at www.nature.com/reprints.
Correspondence and requests for materials should be addressed to Y.F., L.H. or K.L.W.

Competing financial interests

The authors declare no competing financial interests.